Regular Article – Experimental Physics

Hadronic shift in pionic hydrogen

M. Hennebach[1,a], D.F. Anagnostopoulos[2], A. Dax[3], H. Fuhrmann[4], D. Gotta[1,b], A. Gruber[4,c], A. Hirtl[4,c],
P. Indelicato[5,6,7], Y.-W. Liu[3,d], B. Manil[5,e], V.E. Markushin[3,f], A.J. Rusi el Hassani[8], L.M. Simons[3],
M. Trassinelli[9,10], and J. Zmeskal[4]

[1] Institut für Kernphysik, Forschungszentrum Jülich, D-52425 Jülich, Germany
[2] Department of Materials Science and Engineering, University of Ioannina, GR-45110 Ioannina, Greece
[3] Laboratory for Particle Physics, Paul Scherrer Institut, CH-5232 Villigen, Switzerland
[4] Stefan Meyer Institute for Subatomic Physics, Austrian Academy of Sciences, A-1090 Vienna, Austria
[5] Laboratoire Kastler Brossel, Sorbonne Universités, UPMC Univ. Paris 06, Case 74; 4, place Jussieu, 75005 Paris, France
[6] Laboratoire Kastler Brossel, CNRS, 75005, Paris, France
[7] Laboratoire Kastler Brossel, Département de Physique de l'École Normale Supérieure, 24 Rue Lhomond, 75005, Paris, France
[8] Faculté des Sciences et Techniques, Université Abdelmalek Essaâdi, Tanger, Morocco
[9] Institut des NanoSciences de Paris, Sorbonne Universités, UPMC Univ. Paris 06, Case 840; 4, place Jussieu, Paris, France
[10] Institut des NanoSciences de Paris, CNRS, F-75005, Paris, France

Abstract. The hadronic shift in pionic hydrogen has been redetermined to be $\epsilon_{1s} = 7.086 \pm 0.007\text{(stat)} \pm 0.006\text{(sys)}$ eV by X-ray spectroscopy of ground-state transitions applying various energy calibration schemes. The experiment was performed at the high-intensity low-energy pion beam of the Paul Scherrer Institut by using the cyclotron trap and an ultimate-resolution Bragg spectrometer with bent crystals.

1 Introduction

In hadronic atoms, the strong pion-nucleus interaction manifests itself by a change of binding energies and level widths of the low-lying atomic levels. It can be measured in the energies and line widths of the corresponding X-ray transitions when compared to a pure electromagnetically bound system.

Experimentally accessible in the lightest pionic atom —pionic hydrogen (πH)— are the X-ray transitions to the $1s$ ground state, which terminate the atomic de-excitation cascade. Any observed influence of the strong interaction can be attributed fully to the $1s$ state, because hadronic and collisional effects in p states are negligibly small.

---

[a] *Present address*: Areva GmbH, D-63067 Offenbach, Germany.
[b] e-mail: d.gotta@fz-juelich.de (Corresponding author)
[c] *Present address*: Universitätsklinik für Radiologie und Nuklearmedizin, Medizinische Universität Wien, A-1090 Vienna, Austria.
[d] *Present address*: Physics Department, National Tsing Hua University, Hsinchu 300, Taiwan.
[e] *Present address*: Laboratoire de Physique des Lasers, CNRS et Université Paris 13, France.
[f] *Present address*: Department of IT, Paul Scherrer Institut, CH-5232 Villigen, Switzerland.

Hence, the s-level shift and width in πH directly measure the $\pi^- p$ s-wave interaction.

The hadronic level shift in pionic hydrogen is related to the $\pi^- p$ scattering lengths in leading order by the Deser-Goldberger-Baumann-Thirring (DGBT) formula [1]

$$\frac{\epsilon_{1s}}{B_{1s}} = -\frac{4}{r_B} \, a^{LO}_{\pi^- p}. \tag{1}$$

The quantity $a^{LO}_{\pi^- p}$ denotes the scattering length, $B_{1s} = -\alpha^2 \mu c^2/2$ is the Coulomb point-nucleus ground-state binding energy, $r_B = \hbar c/\alpha \mu c^2$ the Bohr radius of the pionic hydrogen atom, and $\mu = m_\pi/(1 + \frac{m_\pi}{m_p})$ the reduced mass of the πH system.

The correction due to the fact, that the πH system is a Coulomb bound state, usually is taken into account by Trueman's expansion in the ratio of scattering length to the Bohr radius [2–5]. In the case of hydrogen ($Z = 1$) it can be expressed up to order $O(\alpha^4)$ and including the logarithmic term as follows [6]:

$$\epsilon_{1s} = \frac{2\alpha^3 \mu^2 c^4}{\hbar c} a_{\pi^- \text{p}}$$
$$\cdot \left[1 - \frac{2\alpha \mu c^2}{\hbar c} (\ln \alpha - 1) \cdot a_{\pi^- \text{p}} + \delta^{\text{vac}}_\epsilon \right]. \tag{2}$$

The term $\delta_\epsilon^{\mathrm{vac}} = 0.48\%$ accounts for the interference of vacuum polarisation and strong interaction [7]. Its uncertainty is assumed to be negligibly small compared to the experimental accuracy [8]. The quantity $a_{\pi^- p}$ then represents the scattering length for two strongly interacting charged particles.

The derivation of the pure hadronic part of scattering lengths is an ongoing effort spanning several decades, both with phenomenological and microscopic approaches. The work is summarized in a recent review, which emphasizes mainly the ansatz of an effective field theory as Chiral Perturbation Theory (χPT) [9]. Recent phenomenological descriptions are given in refs. [10–12].

Within the framework of χPT, the extraction of pure QCD quantities is based on the treatment of strong and electromagnetic isospin violating effects at the same level. At threshold, the two basic parameters of the πN interaction are the isoscalar and isovector s-wave scattering lengths a^+ and a^-. In the limit of isospin conservation and the absence of electric charges, they are given in terms of the elastic reactions $\pi^- p \to \pi^- p$ and $\pi^+ p \to \pi^+ p$ by

$$a^\pm \equiv \frac{1}{2}\left(a_{\pi^- p} \pm a_{\pi^+ p}\right), \qquad (3)$$

i. e., $a_{\pi^- p} = a^+ + a^-$ holds.

The corrections due to strong ($m_u \neq m_d$) and electromagnetic ($Q = e$) isospin violation have been calculated at various levels and approaches [6,8,13]. Numerical values are based on preliminary results for ϵ_{1s} and Γ_{1s} of this experiment [14]. Within the framework of χPT, the most recent determination worked out in next-to-leading order (NLO) is given in refs. [15,16]. The scattering length can be expressed in the form [15–18]

$$a_{\pi^- p} = \left(a^+ + a^-\right) + \triangle a_{\pi^- p}, \qquad (4)$$

where the numerical value of the correction is $\triangle a_{\pi^- p} \approx (-7.7 \pm 3.3) \cdot 10^{-3}\, m_\pi^{-1}$. The uncertainty is dominated ($\pm 3.0 \cdot 10^{-3}\, m_\pi^{-1}$) by the poor knowledge of the low-energy constants (LECs) f_1 and c_1 appearing in leading order of the chiral expansion.

In order to extract the individual scattering length a^+ or a^-, the information obtained from ϵ_{1s} must be combined with the ground-state broadening Γ_{1s}, which depends in leading order only on a^-. In a similar form as given in eq. (2), Γ_{1s} reads [19]

$$\Gamma_{1s} = \frac{4\alpha^3 \mu^2 c^4}{\hbar c}\, q_0 \left(1 + \frac{1}{P}\right)\left(a_{\pi^- p}^{\mathrm{cex}}\right)^2$$
$$\cdot \left[1 - \frac{4\alpha\mu c^2}{\hbar c}(\ln \alpha - 1)\cdot a_{\pi^- p}\right.$$
$$\left. + \frac{2\mu c^4}{(\hbar c)^2}(m_p + m_{\pi^\pm} - m_n - m_{\pi^0})\cdot a_{\pi^0 n}^2 + \delta_\epsilon^{\mathrm{vac}}\right].$$
$$(5)$$

Here, q_0 denotes the center-of-mass momentum of the π^0 and P for pion capture at rest the Panofsky ratio measured to be $P = \frac{\sigma(\pi^- p \to \pi^0 n)}{\sigma(\pi^- p \to \gamma n)} = 1.546 \pm 0.009$ [20]. The scattering length $a_{\pi^0 n}$ is well approximated by a^+ [18].

The QCD quantity a^- is obtained by applying appropriate corrections to the scattering length $a_{\pi^- p}^{\mathrm{cex}}$ of the charge exchange reaction $\pi^- p \to \pi^0 n$:

$$a_{\pi^- p}^{\mathrm{cex}} = -\sqrt{2}\, a^- + \triangle a_{\pi^- p}^{\mathrm{cex}}. \qquad (6)$$

Within the framework of χPT, one obtains $\triangle a_{\pi^- p}^{\mathrm{cex}} = (0.4 \pm 0.9) \cdot 10^{-3}\, m_\pi^{-1}$ [15,16]. The significantly smaller uncertainty is due to the fact that in this case the LECs f_1 and c_1 do not appear in leading order.

Further information on the scattering lengths is obtained from the ground-state shift $\epsilon_{1s}^{\pi\mathrm{D}}$ in pionic deuterium. It is related to the real part of the πD scattering length constituting in leading order the coherent sum of $\pi^- p$ and $\pi^- n$ scattering, which is given by $2 \cdot a^+$. Consequently, the triple $\epsilon_{1s}^{\pi\mathrm{H}}$, $\Gamma_{1s}^{\pi\mathrm{H}}$, and $\epsilon_{1s}^{\pi\mathrm{D}}$ provides a constraint on the two scattering lengths a^+ and a^-. The theoretical framework may be found in refs. [17,18].

Ultimate precision X-ray spectroscopy of pionic and muonic atoms became feasible with the advent of meson factories allowing an efficient use of crystal spectrometers [21]. The measurements described here are part of a series of experiments [22] aiming at a new precision determination of $\epsilon_{1s}^{\pi\mathrm{H}}$, $\Gamma_{1s}^{\pi\mathrm{H}}$, and $\epsilon_{1s}^{\pi\mathrm{D}}$ in order to allow for a decisive constraint on a^+ and a^-. In particular, a comprehensive study of the hadronic line broadening was performed to investigate cascade effects affecting the line width. Therefore, also as an independent check, a study of the cascade-induced line broadening was performed in the twin-system muonic hydrogen [23].

In this experiment, three different transitions to the ground state —$\pi\mathrm{H}(2p-1s)$, $\pi\mathrm{H}(3p-1s)$, and $\pi\mathrm{H}(4p-1s)$ (Kα, Kβ, and Kγ)— have been measured. For energy calibration, both fluorescence and —for the first time— X-rays from exotic atoms were used. The hydrogen density varied from 4 bar to liquid (LH$_2$) in order to study the influence of cascade effects both on X-ray energy and line shape.

This paper reports values for $\epsilon_{1s}^{\pi\mathrm{H}}$ from those measurements for which an energy calibration is available with sufficient accuracy. Results for $\epsilon_{1s}^{\pi\mathrm{D}}$ and $\Gamma_{1s}^{\pi\mathrm{D}}$ are given in detail in refs. [24,25]. Final results of the measurement of $\Gamma_{1s}^{\pi\mathrm{H}}$ will be discussed elsewhere [26]. Preliminary values are given in ref. [14].

2 Atomic cascade

After capture of the pion into atomic states, a quantum cascade starts approximately at principle numbers $n_\pi = 16$ [27]. During this cascade the pionic-hydrogen atom undergoes many collisions with H$_2$ molecules, where de-excitation occurs mainly by (external) Auger electron emission or Coulomb de-excitation. The lower part of the cascade is dominated more and more by X-radiation (fig. 1).

In Auger emission, the released energy is almost completely transferred to the electron because of the mass ratio. In Coulomb de-excitation the πH system encounters a proton in a molecule and the de-excitation energy
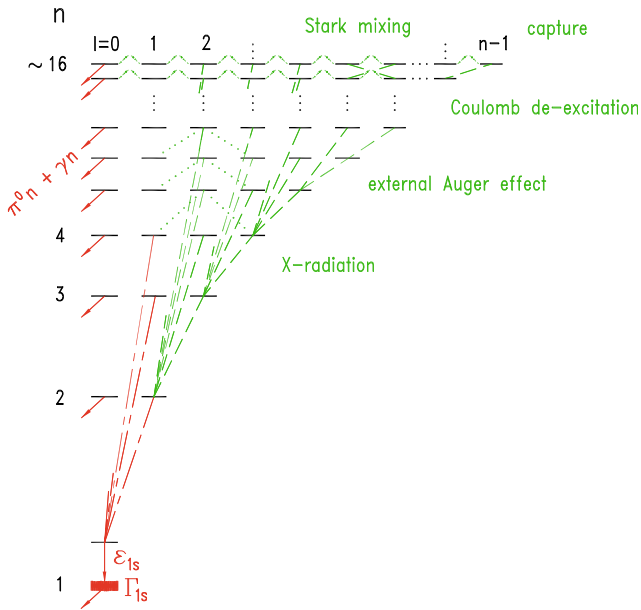
Fig. 1. Atomic de-excitation cascade in pionic hydrogen. Collisional processes and X-radiation dominate the upper and the lower part of the atomic cascade, respectively. X-ray energies of the 3 most intense transitions $\pi H(2p-1s)$, $\pi H(3p-1s)$, and $\pi H(4p-1s)$ are 2.437, 2.885 and 3.043 keV. Hadronic shift ϵ_{1s} and width Γ_{1s} are on the order of $+7$ and 1 eV, respectively. The hadronic shift is defined as $\epsilon_{1s} \equiv E_{\mathrm{exp}} - E_{\mathrm{QED}}$, *i.e.*, a positive sign, as is the case for πH, corresponds to an attractive interaction.

is shared about half and half between the collision partners leading to significant acceleration. The latter process leads to a Doppler broadening which is symmetric and, hence, does not affect the transition energies.

The electrically neutral πH system, being small compared to atomic dimensions, easily penetrates the Coulomb field of the target atoms where the electric field induces transitions between angular momentum states for constant n_π (Stark mixing). Due to the strong interaction the induced s-level width causes the removal of pions from the cascade by the charge exchange $\pi^- p \rightarrow \pi^0 n$ and radiative capture reaction $\pi^- p \rightarrow \gamma n$. This leads to a drastic reduction of the X-ray line yields with increasing target density (Day-Snow-Sucher effect).

Measured line yields for Kα, Kβ, and Kγ lines have been reported for equivalent densities between 3 and 40 bar to be on the order of a few percent [28]. A detailed discussion of the atomic cascade in exotic hydrogen may be found in refs. [29,30].

In order to determine the hadronic shift $\epsilon_{1s}^{\pi H}$ precisely, collision-induced processes causing line shifts must be considered:

  i) Molecular formation of metastable hybrid molecules $[(pp\mu)p]ee$ during $\mu H + H_2$ collisions is well known from the study of muon-catalyzed fusion and muonic hydrogen even at lowest densities and in excited states [31]. During collisions, an analogous process $\pi^- p + H_2 \rightarrow [(pp\pi^-)p]ee$ must be expected [32]. Such complex molecules are assumed to stabilise non-radiatively by Auger emission [33].
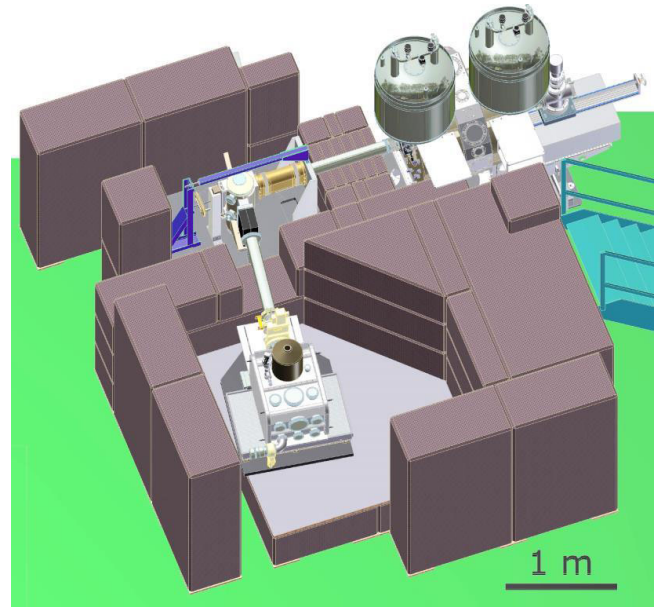

Fig. 2. Set-up of cyclotron trap (top right) and crystal spectrometer in the $\pi E5$ area at PSI for the $\pi H(3p-1s)$ (quartz $10\bar{1}$) and the $\pi H(4p-1s)$ transition (silicon 111). The roof of the concrete cave is not shown.

Possible X-ray transitions from weakly bound molecular states before stabilisation falsify the value for the hadronic shift determined from the measured X-ray energy due to satellite lines shifted to lower energies. In contrast, Auger stabilised molecules emit X-rays of at least 30 eV energy less than the undisturbed transition and are easily resolved in this experiment.

As molecular formation is collision induced, the fraction of formed complex molecules and the X-ray rate would depend on the target density. X-ray transitions from molecular states would show up as low-energy satellites with density dependent intensities because of different collision probabilities. Though radiative decay is predicted to be small in the case of πH [33,34], a measurement of the $\pi H(3p-1s)$ X-ray energy was performed at different densities to possibly identify such radiative contributions.

 ii) The induced energy shift due to Stark broadening has been estimated to be maximal -4 meV at liquid hydrogen density [35]. Consequently, this contribution is neglected at all lower densities.

iii) Estimates on the pressure shift of the X-ray energy yield values less than -0.2 meV at all densities considered.

3 Experimental approach

The experiment used the high intensity pion beam extracted to the $\pi E5$ area at the Paul Scherrer Institute (fig. 2). The average proton current of the accelerator at the pion-production target was between 1.35 and 1.8 mA.
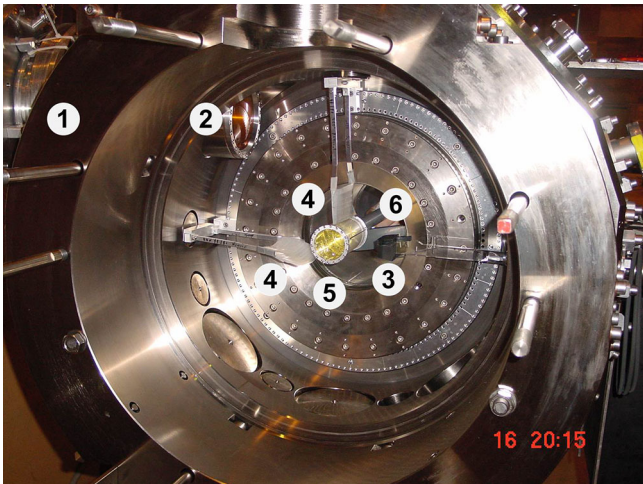
Fig. 3. Installations inside the cyclotron trap. One coil of the magnet assembly is removed. The inner part of the magnetic shielding (iron return yoke) serves as wall for the vacuum chamber containing target cell and degraders. 1) return yoke, 2) beam entrance window, 3) first degrader (38 mm carbonized polyethylene), 4) wedge-shaped secondary degraders (stack of polyethylene foils), 5) gas cell, 6) cooling finger.

The pion beam line was set up to $85\,\mathrm{MeV}/c$ momentum and guided into the cyclotron trap II [36,37]. In the center of the trap a gas-filled cylindrical target cell was placed (fig. 3). A fraction of about 0.5% of the incoming pions was stopped in hydrogen gas per 1 bar equivalent pressure. The cell wall was made of a $75\,\mu$m thick Kapton foil with a diameter of about 59 mm. Its end cap towards the crystal spectrometer contained a $7.5\,\mu$m Kapton window supported either by a stainless steel honeycomb structure or by narrow horizontally oriented aluminum bars.

As a thin Kapton window limits gas pressure to about 2 bar, the hydrogen density was adjusted by means of a cooling finger by temperature variation. In this way, a density range from 4 bar equivalent to liquid (corresponding to 700 bar) was covered. The density of at least 4 bar is necessary in order to achieve a sufficient count rate.

The free length of the target cell's Kapton wall was about 120 mm except for the case $\pi\mathrm{H}(4p-1s)/\mathrm{GaK}\alpha_2$. Here, a cell of 220 mm length was used with a GaAs plate installed inside the gas volume as used for the experiment described in ref. [25]. In the case of the combination $\pi\mathrm{H}(3p-1s)/\pi\mathrm{Be}(4f-3d)$, thin beryllium plates were installed inside the target cylinder. The arrangement was similar to the one outlined in ref. [38] where the $\pi\mathrm{Be}$ line was used to determine the spectrometer response.

The crystal spectrometer was set up in Johann geometry [39]. In this experiment, spherically bent Bragg crystals were used resulting in a partial vertical focussing which increases the count rate. Such a configuration allows the simultaneous measurement of a complete energy interval as given by the extension of the target in the direction of dispersion and when using a detector of corresponding size. In this way, the simultaneous measurement became

possible for the line pairs $\pi\mathrm{H}(3p-1s)/\pi^{16}\mathrm{O}(6h-5g)$ and $\pi\mathrm{H}(3p-1s)/\pi\mathrm{Be}(4f-3d)$ (see table 1).

For X-ray diffraction, a quartz and a silicon crystal was used cut along the $(10\bar{1})$ and (111) plane, respectively. Angular resolutions [40], a possible miscut and its orientation [41] were determined in dedicated experiments. The bending radii of the quartz and the silicon crystal were measured to $R_c = (2980.6 \pm 0.4)$ and $(2982.2 \pm 0.3)\,\mathrm{mm}$ (see footnote[1]). The full diameter of the crystal plates of 100 mm was limited twofold: i) by a spherical aperture to a diameter of 95 mm in order to avoid edge effects and ii) in the direction of dispersion to $\pm 30\,\mathrm{mm}$ to keep Johann broadening small [42].

A 3×2 array $(vertical \times horizontal)$ of charge-coupled devices having a sensitive area of $72 \times 48\,\mathrm{mm}^2$ was used for position-sensitive X-ray detection in two dimensions [43, 44] as in the muonic hydrogen [23] and pionic deuterium experiments [24,25]. The detector's distance from the Bragg crystal is found by the focussing condition $R_c \cdot \sin\theta_{\mathrm{Bragg}}$ corrected for the miscut [41].

The spectrometer was set up inside a massive concrete cave (fig. 2). In this way, beam-induced background, in particular from neutrons, is substantially suppressed. The cave serves, in addition, as (passive) temperature stabilisation. Thus, the temperature was kept stable to about $\pm 1°$ damping the variation in the environment by one order of magnitude. Thermal expansion coefficients of quartz and silicon are $14 \cdot 10^{-6}$ and $2.5 \cdot 10^{-6}$ so that changes of the crystals' lattice constants cause only negligibly small shifts. Details of the interconnections of the chamber housing the Bragg crystal to the cyclotron trap containing the target cell on one side and the cryostat with the X-ray detector are displayed in figs. 4 and 5 of ref. [25].

An accurate determination of the X-ray energy requires both i) sufficient statistics and ii) the possibility to determine the line's center of gravity very precisely. For the $\pi\mathrm{H}$ line a sufficiently high X-ray rate is not achievable at low densities. Because of Stark mixing, liquid hydrogen is also discarded. The best figure of merit is obtained for an equivalent target density between 10 and 30 bar (table 2). Therefore, 30 bar was chosen for a high-statistics measurement of the $\pi\mathrm{H}(3p-1s)$ transition, which spanned about 3 weeks.

During the long-term measurements (labels C and D in table 2) a mechanical shift of the X-ray detector was observed. It resulted in a monotonic position shift of the $\pi\mathrm{H}(3p-1s)$ line. The shift of the $\pi\mathrm{O}(6h-5g)$ calibration line was found to occur synchronously. The line shift was corrected by means of a polynomial ansatz. The uncertainty of the correction ($\pm 4.5\,\mathrm{meV}$) is the largest contribution to the systematic errors of measurements B and D (table 3).

A comprehensive discussion can be found in ref. [45]. The mechanical setup is similar to the one used in the pionic-deuterium experiment and is described in detail in ref. [25].

---

[1] Bragg crystals were manufactured in collaboration with Carl Zeiss AG, D-73447 Oberkochen, Germany.

Table 1. Energies E_X and Bragg angles Θ_{Bragg} for the various combinations of pionic hydrogen and calibration lines. Energies of fluorescence X-rays are taken from [46]. Bragg angles for πH lines are calculated from the final result. The lattice constants are taken to be $2d = (0.6685977 \pm 0.000022)$ nm for (natural) quartz [60] and $2d = (0.62712016 \pm 0.0000001)$ nm for silicon [61] at $T = 25\,^\circ$C. $\triangle\Theta_{IRS}$, $\triangle\Theta_p$, $\triangle\Theta_b$, and $\triangle\Theta_{def}$ are the angular corrections (in seconds of arc) to be applied due to index of refraction, bending, penetration depth, and defocussing (see text).

Crystal	Reflection	Transition	E_X/eV	Θ_{Bragg}	$\triangle\Theta_{IRS}$	$\triangle\Theta_p$	$\triangle\Theta_b$	$\triangle\Theta_{def}$
Quartz	$10\bar{1}$	πH$(3p-1s)$		$39°59'0.3''$	$28.2''$	$-0.11''$	$-1.62''$	0
		π^{18}O$(6h-5g)$	2883.488 ± 0.001	$40°1'26.0''$	$28.2''$	$-0.11''$	$-1.63''$	$0.01''$
		π^{16}O$(6h-5g)$	2880.506 ± 0.001	$40°4'25.4''$	$28.3''$	$-0.11''$	$-1.63''$	$0.03''$
Silicon	111	πH$(3p-1s)$		$43°14'26.6''$	$24.2''$	$-0.09''$	$-4.16''$	0
		π^{16}O$(6h-5g)$	2880.506 ± 0.001	$43°20'31.2''$	$24.3''$	$-0.09''$	$-4.18''$	$0.04''$
		πBe$(4f-3d)$	$2844.064 \pm 0.001^{(a)}$	$44°2'20.0''$	$24.8''$	$-0.09''$	$-4.28''$	$0.46''$
Silicon	111	πH$(3p-1s)$		$43°14'26.6''$	$24.2''$	$-0.09''$	$-4.16''$	0
	333	Zn Kα_1	8638.904 ± 0.073	$43°21'30.1''$	$2.7''$	$-0.44''$	$-4.04''$	$0.05''$
Silicon	333	Ga Kα_2	9224.835 ± 0.027	$40°0'44,1''$	$2.4''$	$-0.50''$	$-3.59''$	0
	111	πH$(4p-1s)$		$40°30'58.4''$	$22.1''$	$-0.10''$	$-3.78''$	$0.31''$

$^{(a)}$ assumes two remaining K and one L electrons.

Table 2. Experimental conditions for the various measurements of πH transitions and calibration lines (labels A–G). Equivalent hydrogen densities are given as pressure values corresponding to a temperature of $20\,^\circ$C (NTP). Counts are results of fits to the line shape.

Label	Transitions hydrogen/calibration	Crystal reflection	Equivalent density H_2/bar	Counts πH/hour	Counts per transition πH	πO, πBe or X-ray
A	πH$(3p-1s)/\pi$O$(6h-5g)^{(a)}$	Si 111/Si 111	4.1 ± 0.1	12.2 ± 0.8	673 ± 45	461 ± 93
B	πH$(3p-1s)/\pi$O$(6h-5g)^{(a)}$	qu $10\bar{1}$/qu $10\bar{1}$	3.8 ± 0.1	17.0 ± 0.7	1004 ± 38	729 ± 30
C	πH$(3p-1s)/\pi$O$(6h-5g)$	qu $10\bar{1}$/qu $10\bar{1}$	29.7 ± 0.6	37.8 ± 0.5	6838 ± 92	6867 ± 91
D	πH$(3p-1s)/\pi$O$(6h-5g)$	qu $10\bar{1}$/qu $10\bar{1}$	LH_2	16.2 ± 0.5	1719 ± 49	693 ± 29
E	πH$(3p-1s)/\pi$Be$(4f-3d)^{(a)}$	Si 111/Si 111	9.3 ± 0.3	22.1 ± 0.9	928 ± 37	1273 ± 39
F	πH$(3p-1s)/$Zn Kα_1	Si 111/Si 333	9.5 ± 0.3	40.0 ± 0.5	7220 ± 96	485380 ± 909
G	πH$(4p-1s)/$Ga Kα_2	Si 111/Si 333	9.9 ± 0.3	14.7 ± 1.2	265 ± 22	2626 ± 59

$^{(a)}$ Simultaneous measurement of πH transition and calibration line.

Table 3. Results from this experiment contributing to the weighted average for the ground-state shift ϵ_{1s} in pionic hydrogen as given in eq. (7) and table 5. $\triangle m_\pi$ denotes the contribution arising from the uncertainty of the pion mass to the error of line energy E_{exp} or hadronic shift ϵ_{1s}.

Label	Transitions hydrogen/calibration	E_{exp} / eV	$\triangle E_{exp}$ stat / eV	sys exp / eV	QED or E_X / eV	$\triangle m_\pi$ / eV	ϵ_{1s} / meV	$\triangle\epsilon_{1s}$ $\triangle m_\pi$ / meV	total / meV
A	πH$(3p-1s)/\pi$O$(6h-5g)$	2885.8777	0.0439	0.0033	0.0014	0.0063	7047.4	0.8	44.1
B	πH$(3p-1s)/\pi$O$(6h-5g)$	2885.9010	0.0314	0.0036	0.0014	0.0063	7070.7	0.8	31.6
C	πH$(3p-1s)/\pi$O$(6h-5g)$	2885.9205	0.0120	0.0055	0.0014	0.0063	7090.2	0.8	13.6
D	πH$(3p-1s)/\pi$O$(6h-5g)$	2885.9160	0.0256	0.0055	0.0014	0.0063	7085.7	0.8	26.2
E	πH$(3p-1s)/\pi$Be$(4f-3d)$	2885.9207	0.0345	0.0045	0.0014	0.0063	7090.6	0.8	34.8
F	πH$(3p-1s)/$Zn Kα_1	2885.9280	0.0108	0.0125	0.073	0.0067	7097.7	6.7	75.1
G	πH$(4p-1s)/$Ga Kα_2	3043.1971	0.0598	0.0097	0.027	0.0067	7105.0	6.7	66.7

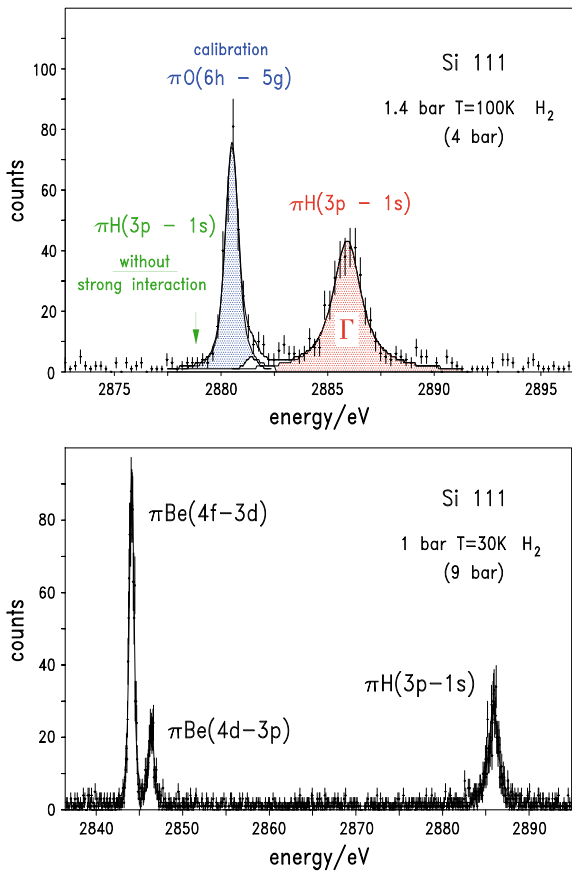**Fig. 4.** Spectra from simultaneous measurements of the $\pi H(3p - 1s)$ transition and the $\pi^{16}O(6h - 5g)$ (top) and the $\pi^{16}Be(4f - 3d)$ calibration lines (bottom).

4 Energy calibration

In the Johann-type setup, the absolute Bragg angle Θ_{Bragg} cannot be determined with sufficient precision. Therefore, calibration is performed relative to a line of known energy with Θ_{Bragg} as close as possible to the πH case. Experimentally, this corresponds to the determination of the angle difference as measured by means of the position difference on the detector (figs. 4 and 5).

In this experimental approach, the energy calibration is performed in two ways:

i) Fluorescence X-rays are well suited for stability monitoring because high rates are available when illuminating suitable materials with commercial X-ray tubes. Here, the Zn Kα_1 and Ga Kα_2 lines are used having almost the same Bragg angle as the $\pi H(3p - 1s)$ and the $\pi H(4p - 1s)$ transition, respectively. However, the Zn and Ga lines have to be measured in third order, whereas the πH transitions are reflected in first order. This requires a substantial correction due to the change of the index of reflection ($\triangle\Theta_{\text{IRS}}$) (table 1). The calibration energy is given by the peak of the fluorescence line, which corresponds to the tabulated value. For Zn, the value was taken from the compilation of Deslattes *et al.* [46]. Energies communicated for Ga X-rays were obtained from the compound GaAs
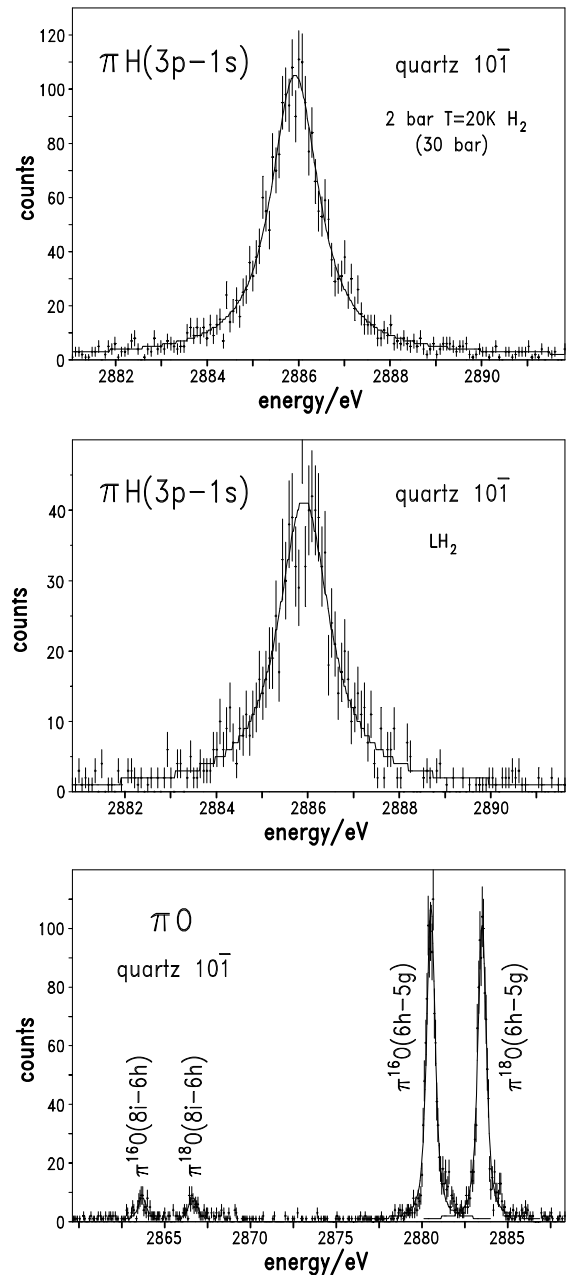

Fig. 5. High-statistics measurement of the $\pi H(3p - 1s)$ transition (top), first crystal spectrometer measurement in liquid hydrogen (middle), and energy calibration with $(6-5)$ transitions from an $^{16}O_2/^{18}O_2$ mix target at 4 bar equivalent density with an 80% He admixture. Also visible are the inner transitions $(8i - 6h)$ of the oxygen isotopes having energies of 2863.689 and 2866.652 eV.

as used in this experiment [47]. However, the precision achievable using fluorescence X-rays is limited due to the large natural width and the line asymmetry because of satellite structures [48]. Hence, these calibrations are mainly regarded as consistency checks.

ii) For the first time, πH transitions were calibrated using X-rays from pionic atoms itself ($\pi O(6h - 5g)$ and $\pi Be(4d - 3p)$) (table 2 and fig. 4) having natural line widths much smaller than Zn or Ga K X-rays. Further-

more, the uncertainty of the pion mass (2.5 ppm) [49] cancels in leading order (see table 3). Important, however, is the use of transitions from the intermediate part of the atomic cascade between circular orbits like $6h - 5g$ or $4f - 3d$, where level energies are not affected by nuclear finite size and, therefore, do not experience a noticeable hadronic shift. Unfortunately, suitable pionic-atom transitions close in energy only exist for the $\pi H(3p - 1s)$ transition.

For gaseous targets, pionic oxygen can be regarded as a hydrogen-like atomic system, because screening effects from remaining electrons are small due to a practically complete removal of the electron shells before the $\pi O(6h - 5g)$ transition occurs [50–52]. Line broadening owing to Coulomb explosion [53] is symmetric and, hence, does not affect the position. Similarly, Doppler broadening caused by Coulomb de-excitation [54,55] can be assumed to be symmetric as well (see, *e. g.*, ref. [30]).

At low density, $\pi O(6 - 5)$ and $\pi H(3p - 1s)$ lines were measured simultaneously by using a hydrogen-oxygen gas mixture of H_2/O_2 (98%/2%) (fig. 4). Higher densities (≥ 10 bar equivalent) require lower temperatures. Hence, hydrogen and oxygen were measured alternately because the oxygen gas freezes out in such conditions. In one of these measurements, a mixture of $^4He/^{16}O_2/^{18}O_2$ (80%/10%/10%) was used (fig. 5). The oxygen isotopes serve as a check for the dispersion of the spectrometer. The admixture of helium reduces self-absorption of X-rays in the oxygen target.

For solid targets, like Be as used here, in contrast to gases, electron screening has been found to be significant [56–58]. Here, a fast electron refilling is expected from the environment restoring electronic shells even during the rapidly proceeding atomic cascade. Moreover, for this mixed target setup H_2/Be the rate is limited because of the predominant absorption in the beryllium plates.

The limiting systematic uncertainty is due to the simultaneous description of the parallel transitions $\pi O(6g - 5f)$ or $\pi Be(4d - 3p)$ contributing to the line shape on the high-energy side. The accuracy in the calculation of the pure electromagnetic transition energy itself is about one meV only [59].

5 Analysis

5.1 Data processing

As discussed in detail in ref. [25], the Bragg reflection of a narrow X-ray line generates a parabolic hit pattern in the detector plane. Analyzing the hit pattern and acceptance of only single- or two-pixel events significantly reduces beam-induced background leading to an excellent peak-to-background ratio (figs. 4 and 5). The curvature of the parabola was fitted to the narrow πO or the high-statistics X-ray fluorescence line and then applied to the corresponding πH transition. The one-dimensional spectrum obtained after projection of the curvature-corrected pattern to the axis of dispersion is equivalent to an energy spectrum.

Table 4. Calculated values for the pure electromagnetic transition energies E_{QED} in πH (from [59]). Values include the energy decrease due to atom recoil.

Transition	$\pi H(3p - 1s)$	$\pi H(4p - 1s)$
E_{QED} / eV	2878.8303 ± 0.0064	3036.0921 ± 0.0068

The position of the reflection is obtained by means of a fit to the line shape using Voigt profiles. Though the spectrometer response is slightly asymmetric, it turned out that using a symmetric profile does affect the lines' position difference by typically 1–2 meV only. For the determination of the hadronic broadening, however, the inclusion of the exact response is mandatory [14,23–25].

Owing to imaging and diffraction properties, corrections must be applied to the line position as obtained from the fit (table 1). Main correction is the above-mentioned index of refraction shift $\triangle\Theta_{IRS}$, in particular, when πH and calibration line are measured in different orders of reflection. Secondly, as penetration depth of the X-radiation differs significantly with energy a corresponding correction has to be applied ($\triangle\Theta_p$). Hence, an additional bending correction is necessary which takes into account the variation of the lattice constant with penetration depth ($\triangle\Theta_b$). We use the approach of Cembali *et al.* [62].

A further correction stems from the different focal lengths of πH and calibration lines ($\triangle\Theta_{def}$). The shift due to this defocussing is approximately linear with the difference in the crystal-to-detector distance.

The uncertainty of $\triangle\Theta_{IRS}$ is on the order of 0.5% [63, 64]. A conservative estimate for the accuracy of $\triangle\Theta_p$ and $\triangle\Theta_b$ is 30% which owes to deviations from the ideal crystal structure in the thin reflecting surface layer. However, for measurements using the same order of reflection only differences of rather small corrections contribute. Therefore, a maximum uncertainty of about 50% for the difference can be assumed. The defocussing correction $\triangle\Theta_{def}$ has been studied by means of Monte Carlo simulation to be precise at least on the level of 20%.

Further possible sources of uncertainties are the accuracy of the curvature correction, the distance of the Bragg crystal to the detector and its alignment and pixel size, as well as temperature stability. The analysis of position monitoring and a survey measurement of the experimental setup yields individual contributions of less than 0.2 meV each. Uncertainties owing to the individual measurements are included in the corresponding systematic error as given in table 3 and are, in particular, due to fit model and long-term stability.

5.2 Electromagnetic transition energies

For pionic hydrogen, the pure electromagnetic transition energies have been recalculated recently [59]. Partly, the results deviate from previous calculations by more than the experimental accuracy (see tables 4 and 5). Additional effects arising from strong interaction and polarisability are discussed below.

Table 5. Comparison of results for the ground-state shift ϵ_{1s} in pionic hydrogen. Values for ϵ_{1s} of previous experiments are given based on the corresponding values for the electromagnetic transition energy E_{QED}, which are different from the most recent result of Schlesser *et al.* [59] as given in the last row. Noteworthy, that all precision experiments are in good agreement when using the same value for the electromagnetic transition energy (see text).

Transition	Equivalent density H_2/bar	Energy calibration	E_{exp} / eV	E_{QED} / eV	ϵ_{1s} / meV	
$\pi H(2p - 1s)$	4	$^{55}Fe/^{65}Zn$	2500 ± 500	2436	–	[68]
$\pi H(2p - 1s)$	18	V Kα_1	2433.5 ± 1.7	2429.6 ± 0.2	3900 ± 1700	[69]
$\pi H(2p - 1s)$	40	V Kα_1	2434.5 ± 0.5	2429.6	4900 ± 500	[70]
$\pi H(3p - 1s)$	15	Ar Kα_1	2885.98 ± 0.23	2878.86 ± 0.03	7120 ± 320	[71]
$\pi H(3p - 1s)$	15	Ar K$\alpha_{1,2}$	2885.935 ± 0.048	2878.808 ± 0.008	7127 ± 46	[38,72]
$\pi H(4p - 1s)$	15	Ga Kα_2	3042.97 ± 0.15	3036.068 ± 0.009	6900 ± 150	[38,72]
$\pi H(3p - 1s)$	15	Ar K$\alpha_{1,2}$	2885.916 ± 0.034	2878.808 ± 0.008	7108 ± 36	[66,67]
Weigthed average of this experiment (for details see table 3)					7085.8 ± 9.6	

The influence of the strong interaction on the $3p$-level energies may be estimated from the sum of the angular-momentum averaged isoscalar and isovector πN p-wave scattering volumes $c_0 + c_1$. Numerical values can be found, *e.g.*, in ref. [65]. Applying the Trueman formula as given by [3,4] results in negligibly small values of 7.4 and 5.8 μeV for the $3p$ and $4p$ state, respectively.

Effects due to the electric and hadronic polarisabilities of proton and pion have been discussed in ref. [59]. The energy shift was found to be (-0.6 ± 0.6) meV. Therefore, this contribution is neglected, too.

6 Results

6.1 Hadronic shift

The results obtained from the individual measurements are consistent within the errors (table 3). Therefore, a weighted average is calculated:

$$\epsilon_{1s} = 7.0858 \pm 0.0071 \,(\text{stat}) \pm 0.0064 \,(\text{sys}) \,\text{eV}. \quad (7)$$

The first error represents the statistical accuracy. The second one includes all systematic effects, which are due to the spectrometer setup, imaging properties of extended Bragg crystals, analysis and instabilities as well as the pion mass. The contribution from the uncertainty of the pion mass cancels in leading order for transitions calibrated with a pionic-atom transition itself (table 3).

The combined result of the most recent previous precision measurements yielded $\epsilon_{1s} = 7.108 \pm 0.036$ eV [66,67], where the energy calibration was performed with argon Kα fluorescence X-rays (the sign convention in refs. [66, 67] is opposite to the one used here). The measured $\pi H(3p - 1s)$ transition energies, however, are in perfect agreement (table 5). Therefore, any discrepancy to the new result vanishes completely when taking into account the newly calculated pure electromagnetic transition energy.
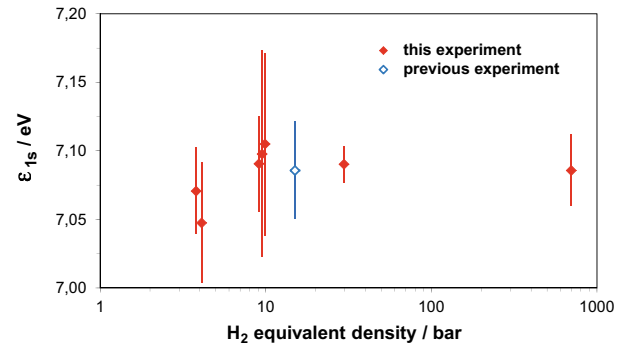

Fig. 6. Results for the hadronic ground-state shift ϵ_{1s} in pionic hydrogen at various H_2 densities ($\blacklozenge$). The open diamond ($\lozenge$) represents the weigthed average of the previous precision experiment [67] when also using the new value for the electromagnetic transition energy. Note the logarithmic scale for the density.

As discussed in sect. 2, a density dependence of the $\pi H(3p - 1s)$ transition energy would be evidence for radiative decay after molecular formation. In this experiment, no evidence is found within the experimental uncertainty between 3.8 bar and liquid (fig. 6), *i.e.*, within a density range of a factor of about 200. A linear fit yields for the slope a value consistent with zero $((0.004 \pm 0.04)$ meV/bar$)$. Consequently, the result for ϵ_{1s} is unaltered when extrapolating to zero density.

Remarkably, the result for the combination $\pi H(3p-1s)/\pi Be(4f - 3d)$ is only consistent with the other measurements when the presence of two K electrons in the πBe system is assumed. The screening correction is calculated to be -143 meV, which is about a factor of 4 larger than the experimental error for the transition energy. A complete refilling of electron shells is expected because capture rates are very high in particular from the conduction band in solid state metals [56]. The influence of an additional L electron screening $(-9$ meV$)$ is beyond the experimental accuracy.

6.2 Scattering length

Using the result given in eq. (7), the Coulomb-corrected strong-interaction $\pi^- p$ scattering length is obtained from eq. (2) to be

$$a_{\pi^- p} = (85.26 \pm 0.12) \cdot 10^{-3} \, m_\pi^{-1}, \qquad (8)$$

which is 1.01% smaller than the LO value when using eq. (1).

The experimental uncertainty for $a_{\pi^- p}$ amounts to 0.14% only. However, applying eq. (4) for the extraction of the QCD quantity $a^+ + a^-$ yields

$$a^+ + a^- = (81.4 \pm 3.6) \cdot 10^{-3} \, m_\pi^{-1}. \qquad (9)$$

The uncertainty is due to the poor knowledge of low-energy constants appearing already in NLO as discussed in detail in refs. [17,18]. The new value for ϵ_{1s} yields a small shift for the isoscalar scattering length from $a^+ = (7.6 \pm 3.1) \cdot 10^{-3} \, m_\pi^{-1}$ to $(7.5 \pm 3.1) \cdot 10^{-3} \, m_\pi^{-1}$ in the analysis of Baru et al. [17,18].

7 Summary

The $\pi^- p$ scattering length has been determined with a precision of 0.14% from various ground-state transitions in pionic hydrogen and applying different energy calibration schemes. The result represents a fourfold improvement compared to the most precise previous experiment [67]. All individual results coincide very well within the experimental uncertainties. The weighted average is in excellent agreement with the previous precision experiment when the updated result for the pure electromagnetic transition energy is applied.

Within the experimental uncertainty, no pressure dependence of the $\pi H(3p - 1s)$ energy could be observed. This excludes, in particular, radiative decay out of molecular bound states, the formation of which is assumed to be density dependent. Any contribution above the 1% level can be discarded.

It is worthwhile to mention that the assumption is confirmed that exotic atoms formed within metallic targets recover electrons after Auger emission on time scales much faster than the cascade time in contrast to gaseous targets. This is revealed by the energy measured for the πBe $(4f - 3d)$ transition, which requires the presence of a complete electronic K shell at the time of the pionic transition.

References

1. S. Deser et al., Phys. Rev. **54**, 774 (1954).
2. T.L. Trueman, Nucl. Phys. **26**, 57 (1961).
3. E. Lambert, Helv. Phys. Acta **42**, 667 (1969).
4. E. Lambert, Helv. Phys. Acta **43**, 713 (1970).
5. J. Mitroy, I.A. Ivallov, J. Phys. G **27**, 1421 (2001).
6. V.E. Lyubovitzkij, A. Rusetski, Phys. Lett. B **494**, 9 (2000).
7. D. Eiras, J. Soto, Phys. Lett. B **491**, 101 (2000).
8. J. Gasser et al., Eur. Phys. J. C **26**, 13 (2002).
9. J. Gasser, V.E. Lyubovitzkij, A. Rusetski, Phys. Rep. **456**, 167 (2008) and references therein.
10. T.E.O. Ericson, B. Loiseau, S. Wycech, Phys. Lett. B **594**, 76 (2004).
11. E. Matsinos, G. Rasche, J. Mod. Phys. **3**, 1369 (2012).
12. E. Matsinos, G. Rasche, Int. J. Mod. Phys. A **28**, 1350039 (2013).
13. V. Bernard et al., Phys. Rev. C **52**, 2185 (1995).
14. D. Gotta et al., Lect. Notes Phys. **745**, 165 (2008).
15. M. Hoferichter, B. Kubis, U.-G. Meißner, Phys. Lett. B **678**, 65 (2009).
16. M. Hoferichter, B. Kubis, U.-G. Meißner, Nucl. Phys. A **883**, 18 (2010).
17. V. Baru et al., Phys. Lett. B **694**, 473 (2011).
18. V. Baru et al., Nucl. Phys. A **872**, 69 (2011).
19. P. Zemp, PhD thesis, University of Bern (2004).
20. J. Spuller et al., Phys. Lett. B **67**, 479 (1977).
21. D. Gotta, Prog. Part. Nucl. Phys. **52**, 133 (2004).
22. PSI proposals R-98.01 and R-06.03, available at `http://collaborations.fz-juelich.de/ikp/exotic-atoms`.
23. D.S. Covita et al., Phys. Rev. Lett. **102**, 023401 (2009).
24. Th. Strauch et al., Phys. Rev. Lett. **104**, 142503 (2010).
25. Th. Strauch et al., Eur. Phys. J. A **47**, 88 (2011).
26. A. Hirtl et al., in preparation.
27. J.S. Cohen, Rep. Prog. Phys. **67**, 1769 (2004).
28. A.J. Rusi el Hassani et al., Z. Phys. A **351**, 113 (1995).
29. F.J. Hartmann, in Proceedings of Physics of Exotic Atoms on Electromagnetic Cascade and Chemistry, Erice, Italy, 1989 (Plenum Press, New York, 1990) p. 23 and p. 127, and references therein.
30. Th.S. Jensen, V.E. Markushin, Lect. Notes Phys. **627**, 37 (2003).
31. M. Diepold et al., Phys. Rev. A **88**, 042520 (2013).
32. S. Jonsell, J. Wallenius, P. Froelich, Phys. Rev. A **59**, 3440 (1999).
33. S. Kilic, J.-P. Karr, L. Hilico, Phys. Rev. A **70**, 042506 (2004).
34. E. Lindroth, J. Wallenius, S. Jonsell, Phys. Rev. A **68**, 032502 (2003) **69**, 059903(E) (2004).
35. Th.S. Jensen, private communication.
36. L.M. Simons, Phys. Scr. **T22**, 90 (1988).

37. L.M. Simons, Hyperfine Interact. **81**, 253 (1993).
38. D. Sigg *et al.*, Nucl. Phys. A **609**, 269 (1996).
39. H.H. Johann, Z. Phys. **69**, 185 (1931).
40. D.F. Anagnostopoulos *et al.*, Nucl. Instrum. Methods A **545**, 217 (2005).
41. D. Covita *et al.*, Rev. Sci. Instrum. **79**, 033102 (2008).
42. J. Eggs, K. Ulmer, Z. Angew. Phys. **20**, 118 (1965).
43. N. Nelms *et al.*, Nucl. Instrum. Methods A **484**, 419 (2002).
44. P. Indelicato *et al.*, Rev. Sci. Instrum. **77**, 043107 (2006).
45. M. Hennebach, *Precision measurement of ground state transitions in pionic hydrogen*, PhD thesis, Universität zu Köln (2003) `http://kups.ub.uni-koeln.de/744/`.
46. R. Deslattes *et al.*, Rev. Mod. Phys. **75**, 35 (2003).
47. T. Mooney, Argonne National Laboratory, private communication.
48. D.F. Anagnostopoulos *et al.*, Phys. Rev. A **60**, 2018 (1999).
49. Particle Data Group (J. Beringer *et al.*), Phys. Rev. D **86**, 010001 (2012).
50. R. Bacher *et al.*, Phys. Rev. A **39**, 1610 (1989).
51. K. Kirch *et al.*, Phys. Rev. A **59**, 3375 (1999).
52. D.F. Anagnostopoulos *et al.*, Phys. Rev. Lett. **91**, 240801 (2003).
53. T. Siems *et al.*, Phys. Rev. Lett. **84**, 4573 (2000).
54. L. Bracci, G. Fiorentini, Nuovo Cimento A **43**, 9 (1978).
55. A. Badertscher *et al.*, Europhys. Lett. **54**, 313 (2001).
56. R. Bacher *et al.*, Phys. Rev. Lett. **54**, 2087 (1985).
57. B. Jeckelmann, P.F.A. Goudsmit, J. Leisi, Phys. Lett. B **335**, 326 (1994).
58. S. Lenz *et al.*, Nucl. Phys. B **416**, 50 (1998).
59. S. Schlesser *et al.*, Phys. Rev. C **84**, 015211 (2011).
60. J.C. Brice, J. Mater. Sci. **15**, 161 (1980).
61. G. Basile *et al.*, Phys. Rev. Lett. **72**, 3133 (1994).
62. F. Cembali *et al.*, J. Appl. Cryst. **25**, 424 (1992).
63. B.L. Henke, E.M. Gullikson, J.C. Davies, At. Data Nucl. Data Tables **54**, 181 (1993).
64. C.T. Chantler, J. Phys. Chem. Ref. Data **24**, 71 (1995).
65. R. Koch, Nucl. Phys. A **448**, 707 (1986).
66. H.-Ch. Schröder *et al.*, Phys. Lett. B **469**, 25 (1999).
67. H.-Ch. Schröder *et al.*, Eur. Phys. J. C **21**, 433 (2001).
68. J. Bailey *et al.*, Phys. Lett. B **32**, 369 (1970).
69. A. Foster *et al.*, Phys. Rev. C **28**, 2374 (1983).
70. E. Bovet *et al.*, Phys. Lett. B **135**, 231 (1985).
71. W. Beer *et al.*, Phys. Lett. B **261**, 16 (1991).
72. D. Sigg *et al.*, Phys. Rev. Lett. **75**, 3245 (1995).